

Vanni Consumi¹, Jeref Merlin¹, Lukas Lindenroth¹ *Member, IEEE*,
Danail Stoyanov¹ *Member, IEEE* and Agostino Stilli¹ *Member, IEEE*

A Novel Soft Shape-shifting Robot with Track-based Locomotion for In-pipe Inspection

Abstract— With the advent of soft robotics the research community has been exploring how to exploit the inherent adaptability of soft elastic materials to overcome the limitations of systems based on rigid materials. A proof-of-concept design of a crawling robot for pipe inspection and preliminary analysis of its locomotion capabilities are presented in this work. The novelty of the proposed design is the combination of silicone-based elements of different stiffness to enable global shape reconfiguration and whole-body track-based locomotion. The proposed system makes use of a plurality of multi-materials elastic tracks actuated by an on-board motor through a worm gear that pairs with all of them, causing their constant eversion from the inside to the outside of the chassis of the robot. Two toroidal inflatable chambers surround the chassis of the robot while passing through the loops created by the tracks. Upon inflation of the chambers the tracks are deformed, changing the overall diameter of the system. This feature allows the system to adjust to the local diameter of the pipe navigated, enabling also active contact force control between the tracks and the pipe walls. We demonstrate how the proposed system efficiently moves through rigid pipes of different diameters, both straight and curved, incrementing its outer diameter up to 100% of his original size. Maximum navigation speed and stall force applied are evaluated. With two front cameras embedded, the proposed robotic system can represent a cost-effective and easy-to-control solution for inspection applications, when adaptability and compliance are critical requirements.

I. INTRODUCTION

Pipe investigation plays a crucial role in intervening quickly and non-invasively when adverse conditions affect the operation of a pipe system. Researchers developed robotic solutions to investigate the inside of pipes through the use of sensors [1] and attempted to efficiently solve challenges associated with the navigation of pipes that change in diameter and slope, embed elbows of different angles, fork in multiple branches, present complex internal geometries or uneven surface.

When designing in-pipe robots, different locomotion approaches have been investigated, with bio-inspiration playing a significant role [2][3][4]. Active motion principles, meaning that the robot carries its own power source (usually motors) and can control its speed, mainly relate to wheeled [5], track-based [6], inchworm [7], legged [8], and snake-type robots [9]. In particular, robots equipped with a wall-pressing mechanism control the traction force by increasing the friction, demonstrating typically better performances and capability to climb vertically.

Furthermore, the development of recent soft robotic approaches based on intrinsically compliant or even stiffness-

¹Vanni Consumi, Jeref Merlin, Lukas Lindenroth, Danail Stoyanov and Agostino Stilli are with the Wellcome/EPSRC Centre for Interventional and Surgical Sciences (WEISS), University College London, London W1W 7EJ, UK (e-mail: vanni.consumi.20@ucl.ac.uk, jeref.merlin.18@ucl.ac.uk, l.lindenroth@ucl.ac.uk, danail.stoyanov@ucl.ac.uk, a.stilli@ucl.ac.uk).

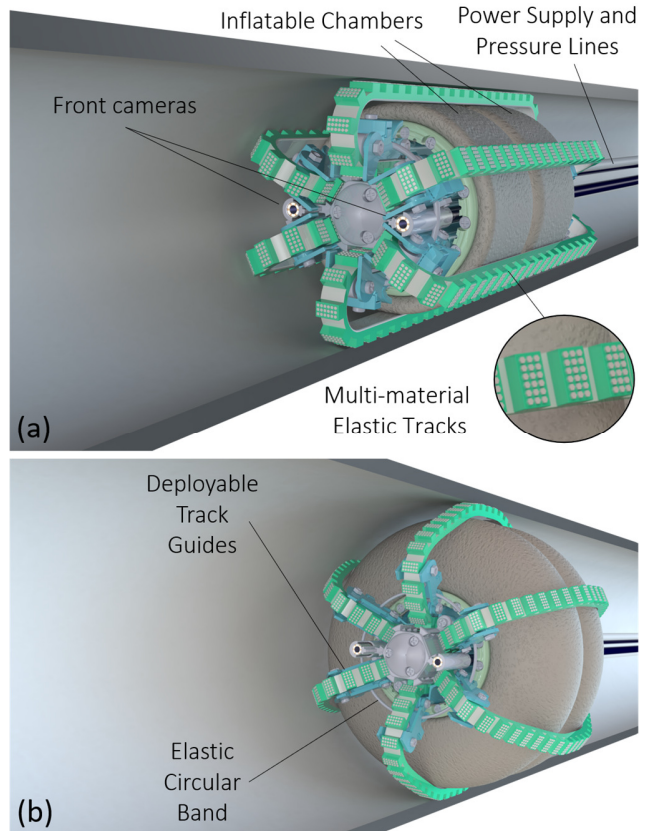


Figure 1 – Renderings of the proposed robot uninflated (a) and inflated (b) inside pipes of different diameters. The crawling motion is obtained by the continuous eversion of 6 elastic tracks made of silicone in contact with the internal wall of the pipe. The tracks are located symmetrically around 2 inflatable chambers that the robot can inflate to enlarge its diameter accordingly with the diameter of the pipe, allowing the tracks to fully contact the surrounding space when the pipe diameter increases. Additionally, the robot embeds two front cameras to perform inside imaging of the pipe.

tunable elements are being investigated more and more by the research community due to their adaptability to unstructured and complex environments [10]. The development of novel soft actuators [11] resulted in the design of soft robotic systems for climbing tasks [12].

Active wheeled robots [13][14][5] have been investigated in this context. Typically, these systems embed six wheels (or six pairs) along the circumferential perimeter of a capsule shaped chassis to enable stable navigation and an active wall-pressing mechanism is used to ensure homogeneous contact with the navigated lumen. In-pipe robots based on screw drive wheels [15][16][17] can also achieve very compact designs with a smaller number of motors. The potential for downscaling of these designs has been demonstrated in [18] where a robot capable of navigating a 25 mm diameter pipe is presented.

Differently from wheel-based robots, track-based robots [19][20][6] exhibit greater contact surface and thus larger traction force and continuous adaptability to uneven and rugged surfaces. Yet, reconfigurable robots such [21][22][23][9] have multiple units and links used to adapt to a wide range of diameters, although, their structure has large length-to-diameter ratio and requires a more complex design and control strategy.

Bio-inspired designs like inchworm robots can achieve navigation by a cycle of expansion and contraction phases [7][24]. Small-scale robotic inchworms can operate in small pipes, however, they suffer of low speeds due to their slow actuation system, i.e., low voltage piezo stack or SMA (shape memory actuation) [25][26]. Pneumatically actuated soft inchworm robots [27][28][29][30][31] rely instead on the inflation of silicone chambers to actively control the diameter of the robot in a wide range of sizes with a relatively simple design, low fabrication costs, and without using on-board motors. Design challenges involve undesired deformation of the chambers and lack of control of the contact pressure: springs [29] or fibre reinforcement [27] are often used to constraint and shape the deformation of the chambers.

Worm gear drive mechanisms combined with tracked or wheeled locomotion have shown potential to be an efficient solution when designing a small robot for active in-pipe navigation using a single actuator [32][33]. The underactuated system based on elastic tracks proposed in [33] has the potential to enable flexible in-pipe navigation, nonetheless, the lack of active control on the contact force between tracks and lumen walls represents the main limitation of this promising design. Since traction has high impact on the motion of a mobile system, larger adhesive force are typically obtained in crawling robots by features such as micro-patterned tracks [34] or micro legs [35][36].

In this paper, we propose a novel design of a soft shape-shifting capsule robot based on constant eversion of elastic tracks for in-pipe locomotion and inspection. The proposed design integrates soft materials both for locomotion and shape reconfiguration. The locomotion principle is based on the continuous eversion of multiple elastic tracks from the inside of the chassis of the robot, a movement enabled by a single rotational actuator paired with a worm gear directly engaging with all the tracks. This track-based approach is combined with a pneumatically actuated wall-pressing mechanism composed by two toroidal inflatable chambers surrounding the chassis. The inflation of these chambers causes the displacement and elastic deformation of the tracks to create track-to-wall contact, thus ensuring the generation and control of the contact friction force that provides traction to the system. With the proposed design we aim at developing an in-pipe robot that is:

- Capable of inspecting pipes with variable diameter.
- Inherently adaptable to uneven surfaces and obstacles.
- Capable of stable and easy-to-control imaging of the navigated pipe.

This paper is organized as follow: Section II details on the locomotion mechanism, a Finite Element analysis (FEA) to characterize the main design challenges of the system and discusses the design solution adopted. Section III demonstrates experimentally the locomotion capabilities of the proof of concept, validating the proposed locomotion principle and

shape-shifting capabilities of the system. In Section IV conclusions and future work are discussed.

II. MATERIAL AND METHODS

A. Locomotion principle and mechanism analysis

The proposed design is presented in Fig. 1, but the key functional elements that we envisioned for this system at the beginning of the design process were only: a rigid cylindrical hollow chassis; a set of elastic toothed tracks regularly spaced along the lateral surface of the chassis running to guarantee 360-degrees contact with the wall of the navigated lumen; two inflatable toroidal chambers placed between the chassis and tracks to displace them in order to enable changing in the overall diameter of the system; and a worm gear that directly engages with the teeth of the tracks while being put in rotation by an electric motor, located inside the chassis.

The combination of these elements allows to move the tracks back or forward based on the direction of rotation of the worm-gear as well as to adjust the diameter of the system to much different pipe diameter ensuring contact of all the tracks while taking advantage of an extremely compact design.

The locomotion principle and mechanism of the proposed system can be summarised as follows:

- Tracks are internally constrained to move linearly along longitudinal guides.
- The force applied by the rotation of the worm gear causes the linear motion of the tracks inside the chassis.
- The internal smooth surface of each track slides on the lateral surfaces of the chambers with minimal friction.
- The external toothed surface is instead in contact with the walls of the navigated pipe.
- The inflation of the chambers displaces and deforms elastically the tracks putting them in contact with the walls of the pipe.
- The contact friction between the external wall and the toothed surface of the tracks generates the force needed to propel the system.
- The direction of motion of the system is the same as the direction of motion of the tracks inside the chassis.

The wall-pressing mechanism of the proposed system consists of two inflatable toroidal chambers longitudinally arranged along the central axis of the robot, as shown in Fig. 1: by inflating the two chambers, the robot can control the normal force applied by the tracks on the walls as well as how many tracks are simultaneously in contact. The novel double-chamber design proposed in this work results in the tracks being suspended between the two most external circumferential profiles of the chambers when inflation takes place. Furthermore, the straight suspended portion of the tracks shapes the overall external surface of the central part of the system in a cylinder, thus offering a surface that can match exactly the internal cylindrical surface of the lumen navigated while also aligning the axis of symmetry of the system with the lumen central axis.

Dynamics of the worm gear driving mechanism of the proposed system is detailed in Appendix section and refers to Fig 2a. In Fig. 2b the same schematic representation of Fig. 2a is used to show all the forces interacting between the moving elements of the system and the pipe navigated. Considering

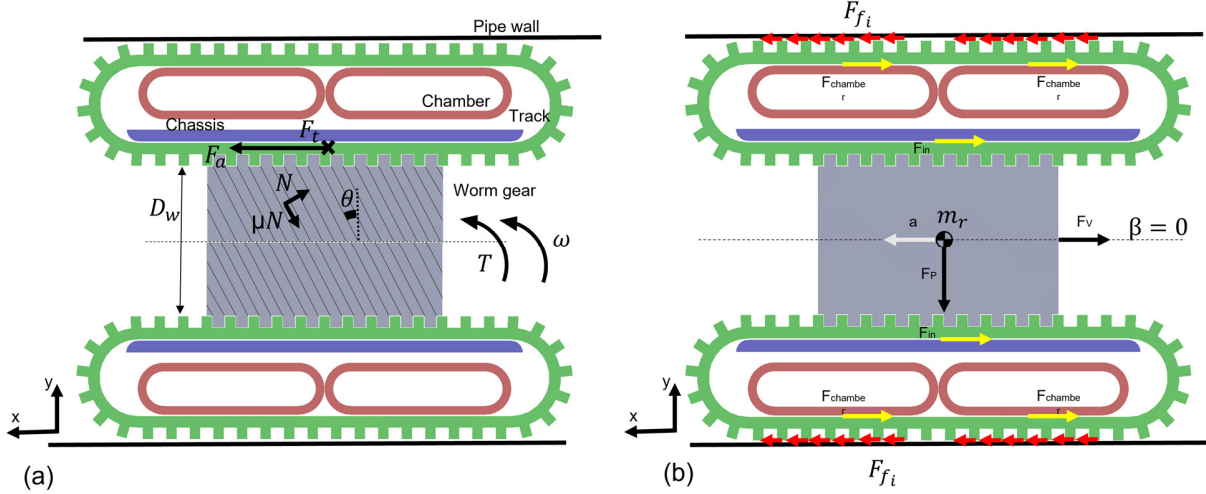


Figure 2 – (a) Configuration of the forces and members involved in the locomotion mechanism: the driving member (worm gear) rotates and moves the driven member (track). (b) Dynamics scheme of the robot: the sum of the static friction forces overcomes the internal dissipating forces and propels the robot.

the system in Fig 2.b having a mass m_r , when it traverses a pipe with inclination β with respect to the horizontal, the dynamics of the centre of mass along the longitudinal axis can be described as:

$$m_r a = n_t F_f - F_{in} - F_{track}(k) - F_{chamber} - F_v + F_p \sin \beta \quad (1)$$

$$F_f = \sum_{i=1}^m F_{f_i} \quad (2)$$

Where n_t is the number of tracks in contact with the wall, F_f is the vectorial sum of the friction forces between the heads of the m teeth that are contact with the wall and the wall itself, F_{in} is the internal dissipation force associated with the friction between tracks and linear guides inside the chassis, $F_{track}(k)$ is the elastic resistance of the tracks and it is function of the elastic constant k of the deformable material used for the tracks, $F_{chamber}$ represents the friction force between the surface of the chambers and the tracks the magnitude of which is function of the normal force between the moving members and F_v is the resistance force on the robot associated with the mass of the cables and pipes dragged by the robot. Lastly, F_p is the gravity component acting on the system that is function of the inclination angle β of the pipe. In an ideal scenario the toothed surface of the track and the walls of the pipe navigated are in a no-slip interaction. The no slip condition stands as long as:

$$F_f < \mu_{tot} F_{chamber} \quad (3)$$

Where μ_{tot} is the static friction coefficient experienced by the track being in contact with the wall and chambers, $F_{chamber}$ is the pressing force that the chamber exerts on the tracks.

B. Finite Element analysis

Since the proposed robot is capable to change its diameter thanks to the two chambers expanding when inflated by pressurized air, the overall shape assumed by the robot is a

crucial design point; in particular, we aim at achieving a high ratio between the radial and the axial deformation of the chambers as a large axial deformation can cause the increase of the chambers' volume at the extremities of the chassis leading to an overall increase in the contact surface between the tracks and the chambers, paired with an additional undesired deformation of the tracks. Ultimately, this results in an increase in the friction losses of the system.

To produce anisotropic deformations in inflatable elastic elements, either additional springs or fibers can be used as reinforcement, or the design of the chambers can embed walls of inhomogeneous thickness to offer different mechanical resistance in different points of the chambers, as exploited in system like the “pneu-net”, where a thin wall encourages the expansion, and a thick wall limits the stretch [37].

In this context, a preliminary design study using Finite Element Analysis (FEA) has been conducted with the software ANSYS™ 2019 (ANSYS Inc., Canonsburg, PA, US), aiming at an optimized design of the chambers to achieve high radial deformation with little volumetric increment at the extremities of the system. Previous FEA investigation carried out in [38] showed the design of a curved chamber to reduce the concentration of von-Mises stress arising throughout a simulated inflation. Starting from there, we analyse by software how different geometries and lengths of the inflatable chambers result on stress, lateral and radial deformation, contact pressure and contact area of the system.

For this study, we consider a planar section of a single track being deformed by the inflation of the two chambers, with no external wall considered. The study compares nine different chamber arrangements as presented in Fig. 3, obtained by the combination of two design features:

1. The locations of the flanges used to airtightly fix the two chambers on the chassis.
2. The ratio (B/C) between the combined axial length of the two chambers and the axial length of the chassis.

The materials used in this work are silicones supplied by Smooth-On Inc., Macungie, PA, US. For each silicone used in the FEA, engineering strain and stress data of uniaxial tensile test were obtained from [39], inserted in the software and fitted with Ogden 1st order hyper-elastic model.

	Internal flanges	Central flanges	External flanges
90% B/C			
75% B/C			
60% B/C			

Figure 3 – Nine configurations evaluated in the FEA study with Ansys 2019®. Planar 2D case of study considers a single track, two chambers and the chassis, considered as a straight monolithic piece. The middle point of segment B/2 (axial length of the single chamber) is always located in the middle of the C/2 segment. The position of the flange that connects the chambers on the chassis and the overall axial length of the balloon with respect to the length of the chassis (B/C factor) vary from (left to right): internal flange, central flange and external flange. Starting from the top to bottom: 90% B/C, 75% B/C and 60% B/C. The position of the flange of the chamber corresponds to the position of the inflating air inlet.

Two cases of study are conducted, with different silicones considered (the rigid chassis is always made of steel): in the first case, chambers and track are made of FX-Pro™ (2A shore hardness); in the second one, chambers and track are composed of DragonSkin20™ (20A shore hardness).

Results for each configuration of both DragonSkin20™ and FX-Pro™ showed the equivalent stress to decrease with the increasing of the volume percentage B/C (Fig. 4a), whereas the maximum contact pressure overall the system is concentrated at the terminal edges of the chassis as the tracks tend to press against chassis' profile due to the lift up effect of the chambers (Fig. 4b).

Interestingly, in both the external and internal flange configurations, the axial deformation of the chambers measured is null in proximity of the position of the flange, meaning that the position of the flange is a local constrain to the axial deformation. Lastly, if we look at the interaction between chambers and track only (Table 1), we see that a configuration with external flange leads to a small contact pressure between track and chambers, (it decreases for high values of the B/C ratio), while an internal flange position shows a smaller contact area (larger contact area arises with higher B/C%). In the real application scenario, smaller contact area is preferable because it means the track is less conformed to the rounded shape of the inflated chamber, while large

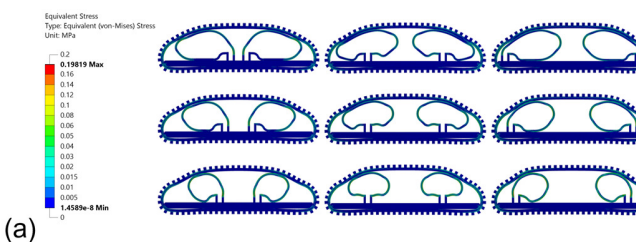
contact pressures are undesirable because they lead to high frictional losses.

From the FEA, we conclude that the use of chambers occupying 60% of B/C is preferred since the mechanical stress arising in the silicone is limited and that the flange's configuration defined as “external” in Fig. 3 can represents a design solution to minimise the axial deformation of the chambers; lastly, the concentration of contact pressure at the edges of the chassis means that an inevitable source of friction arises during the inflation of the system and, for this reason, it suggests the use of a reconfigurable mechanism in this location to ease the mechanical constrain given by a rigid chassis.

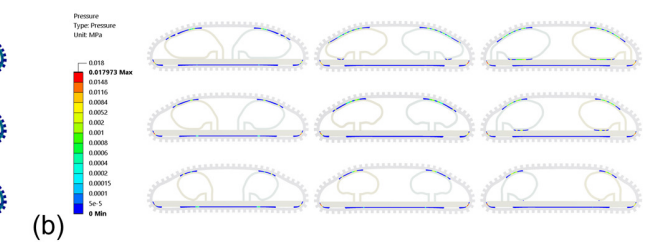
C. Design and fabrication

Based on the locomotion analysis and the FEA of the mechanism presented in sections II.A and II.B, we developed the proof-of-concept system that is presented in Fig. 1a and 1b in perspective view when navigating two pipes of different diameter and in section, front, and rear view in Fig. 5.

The robot's core is composed of a central, rigid, cylindrical body, which encases the gearhead motor (a DC brushless motor 315170 with 256:1 ratio gearbox and rotatory encoder from Maxon Motor™, Sashseln, Switzerland) and the driving screw (Fig. 5a). Rigid components are 3D printed with



(a)



(b)

Figure 4 – Equivalent stress distribution (a) and contact pressure distribution (b) for chambers and tracks made of Dragon Skin™20. Stress magnitude is linked to the risk of failure of the material while contact pressure outlines how the ballooning is taking place. For both figures, starting from left to right the configurations are named as follows: internal flange, central flange and external flange; starting from the top to bottom: 90% B/C, 75% B/C and 60% B/C. Two materials for both track and chambers are investigated in FEA study at a time: chambers and track are made by FX-Pro™ (shore hardness 2 A) in the first case and by DragonSkin20™ (shore hardness 20 A) in the second one. Chassis is made of steel in each case. All the configurations are evaluated for a maximum radial deformation of 14.5 mm. Either materials are suitable to withstand the inflation, the maximum stress measured (Von Mises) is below the tensile stress of the material: maximum stress for DragonSkin20™ is at the 60% B/C and external flange configuration, and corresponds to 5% the tensile stress (3.8 MPa); the maximum stress for FX-Pro™ is measured at the 90% B/C and central flange configuration and corresponds to 4.2% the tensile stress (1.9 MPa). Maximum pressure contact is located at the terminal edges of the chassis for all the configurations: in this location the tracks press on the chassis due to the push up effect of the chambers.

Table 1- Number of elements of the mesh of the chambers in contact with the tracks and contact pressure between tracks and chambers during the inflation in the FEA, for each flange position expressed as ratio B/C (see Fig. 3) where B is the axial space occupied by the chambers and C is the overall length of the chassis in three different configurations (60%, 75%, 90%).

Flange location	Number of contacting			Contact pressure [kPa]		
	60%	75%	90%	60%	75%	90%
Internal	12	20	33	11.13	10.39	10.93
Central	26	59	85	9.68	10.72	11.48
External	29	60	88	3.39	2.23	1.49

Form 3 and Clear Resin (Formlabs™, Somerville, MA, US) and silicone parts are fabricated using injection moulding.

Aiming at both reducing the frictional losses when the robot is moving and increasing the robot shape-shifting capability, a number of design considerations have been made.

As shown in Fig 5b, ball bearings are placed along each internal track guide to reduce the sliding friction happening between the non-toothed surface of the tracks and the surface of the guides inside the chassis, reducing F_{in} components in equation (1). Furthermore, friction coefficient of the silicone-based elastic elements is reduced by using additive SLIDE™ STD (Smooth-On Inc., Macungie, PA, US) during fabrication to significantly reduce the friction losses (F_{in} and $F_{chamber}$) due to relative rubbing such that between track and lateral walls of each guide, between the teeth of the tracks and the worm gear, between the tracks and the chambers.

The terminal parts of the internal guides embedded in the chassis have been designed to provide a certain degree of

compliance to the deformation of the chambers and of the tracks by means of twelve deployable track guides mounted at the six entry and exit points of the tracks as shown in the Fig. 5c. These guides are designed to extend radially if sufficient force is applied by the tracks once they are stretched by the deformation of the chambers as shown in Fig. 6 where four level of inflation are presented. When the chambers are in a not inflated state, these deployable track guides stay closed following the straight profile of the internal portion of the guide thanks to two elastic bands, each wrapping six of the twelve deployable guides.

Differently from the straight and monolithic chassis observed in FEA, this compliant design of the chassis is expected to reduce the concentration of contact pressure at the terminal edges of the chassis and so, the stretch on the tracks, reducing $F_{chamber}$. Since the inflatable chambers are designed with the “external” configuration depicted in Fig. 3, the deformation of the chambers is physically limited to the space comprised between the two flanges thus, the movable terminals, being installed beyond the flanges, are not obstructed in their deployment by the inflating chambers. Lastly, use of Spandex fabric is possible in this design – a membrane is inserted between tracks and chambers and fixed at the distal extremity of each movable terminal. Thanks to its smooth surface and its elastic behaviour it has been successfully used to reduce the silicone-silicone frictional loss without affecting the shape-shifting capabilities of the system.

As shown in Fig. 1 and Fig. 5, the proof-of-concept system embeds two endoscopic cameras (3.5 mm diameter) and LED lighting to provide a full field of view that can be maintained at the centre of the navigated pipe by the self-centring feature given by the two inflating chambers; nonetheless, the pressure control of the chambers is independent thanks to the two air channels routed through the chassis so the user can easily

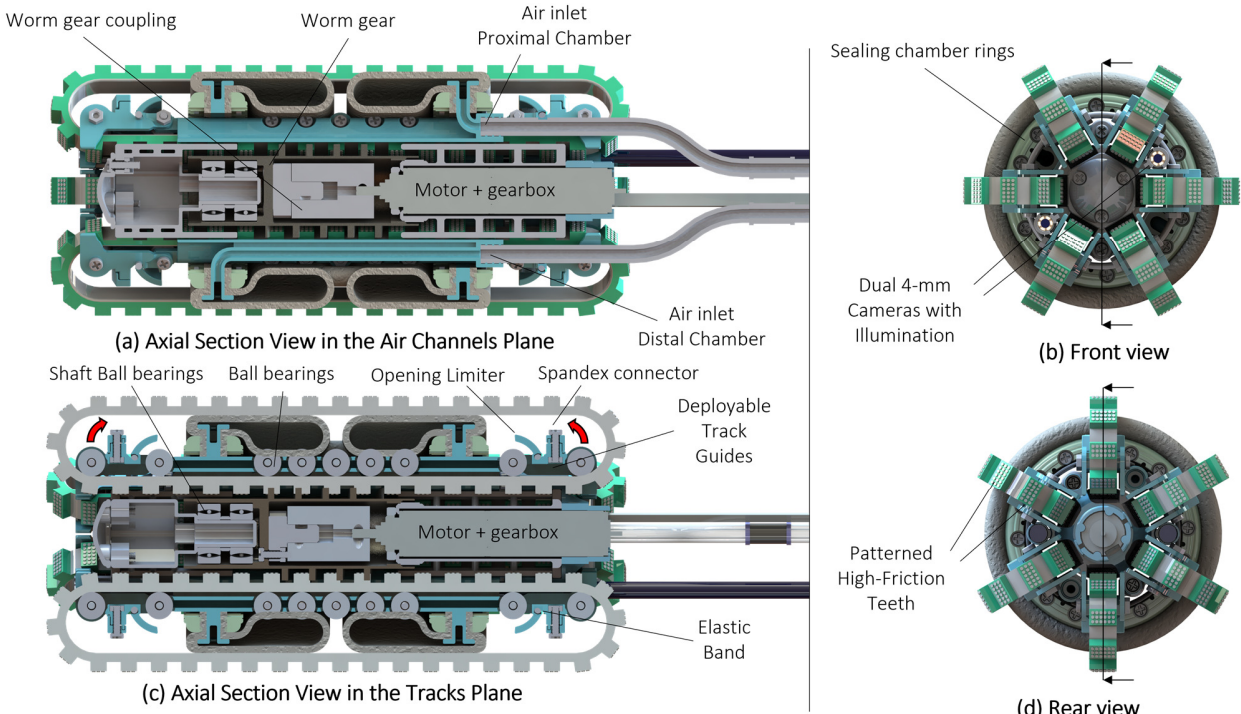


Figure 5 – Front view, section of the air channels, rear view, section of track lanes. Red arrows in axial section highlight the rotation of the deployable links. The two chambers are secured to the chassis using two sets of two gaskets fixed to the flanges with bolts.

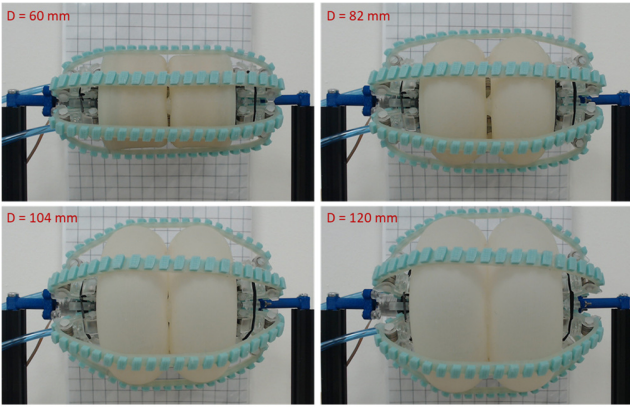


Figure 6 – Various stages of inflation of the elastic chambers. In the top left picture, the robot is not inflated, and the deployable links stay closed thanks to two elastic bands. When the chambers inflate, a pushing force acts on the tracks due to the inflation and the links open radially, releasing the tension on the tracks. As shown in the bottom right picture, the robot is able to reach double of its initial diameter. Note that, additionally, spandex fabric can be secured to these pivoting terminals of the chassis to wrap the external side of the system and thus create a low frictional middle interface in the track-chamber contact (spandex fabric not used in this figure).

control the angle of the optical axis of the cameras with respect to the longitudinal axis of the pipe.

Given the mechanical properties of silicone materials presented in [29], we selected the elastic materials of our system considering that chambers must be stiff enough to deform the tracks while expanding, whereas the tracks must be elastic but still capable of transmitting mechanical power to enable locomotion (the effect of $F_{track}(k)$ depends mostly on the stiffness of the non-toothed portion of the track). For this reason, tracks are manufactured over-moulding and merging three different silicones as shown in Fig. 7: a coating layer with a micro pattern on the top of each tooth made of FX-Pro™ is adopted to locally increase the friction coefficient, thus, the traction force.

In the control set up system presented in Fig. 8, the motor is driven via the motor driver DEC Module 24/2 connected to DEC Module Evaluation Board (Maxon Motor™, Sashseln, Switzerland) and the chambers inflated through two VPPX pressure regulators (FESTO™, Esslingen am Neckar, Germany). Initial testing of the proof-of-concept system has been conducted in open loop control: the user sets the voltage magnitude and direction of the motor, and the pressure of the

Table 2- Average pressure value in the two chambers (front and back) for different inflation levels. Each value is obtained by averaging the pressure readings over five experiments for vertical in-pipe locomotion and horizontal in-pipe locomotion.

Diameter external pipe [mm]	Pressure of chambers (front – back) [kPa]
64	6 – 7
74	17 – 15
84	22 – 23
94	26 – 27

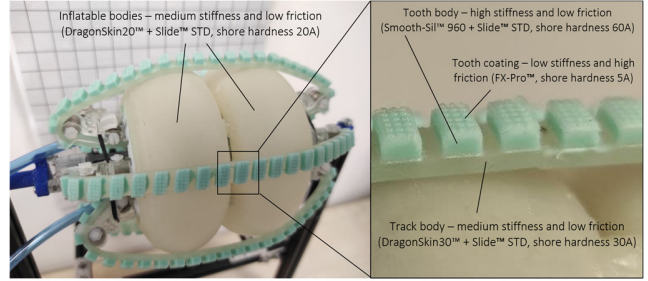


Figure 8 – Materials used for the design of the robot. Inflatable chambers must be considerably stiff when inflated and low frictional to ease mutual sliding, DragonSkin20™ and Slide™ STD additive were selected. Tracks' body must guarantee elasticity and power transmissibility and teeth must be hard enough to ensure power transmissibility when matching the driving screw. DragonSkin30™ is used for the body and Smooth-Sil™ 960 for the tooth fabrication; both are treated with Slide™ STD additive. The top side of the tooth is coated with micro-patterned layer of soft silicone to increase the frictional coefficient of the tracks on the wall pipe; FX-Pro™ is here selected. These three different silicones are combined into a single component with the overmoulding technique.

two chambers. Output pressure signals and motor speed are then captured via Arduino UNO board (10-bit resolution).

III. RESULTS

A. In-pipe locomotion performances

The capabilities of the robot are evaluated inside a set of acrylic pipes of different dimensions, ranging from 64 mm to 94 mm diameter at 10 mm intervals, with the robot measuring 60 mm in the non-inflated configuration. Both vertical and horizontal navigation are tested: speed is measured on upward and downward vertical locomotion, forward and backward horizontal locomotion, over five consecutive tests for each pipe diameter. The maximum navigation speed of the robot is achieved when the motor runs at circa 12000 RPM. The results of these tests are presented in Fig. 9a.

The system is able of navigating inside straight pipes keeping the tracks in contact with the wall, increasing its

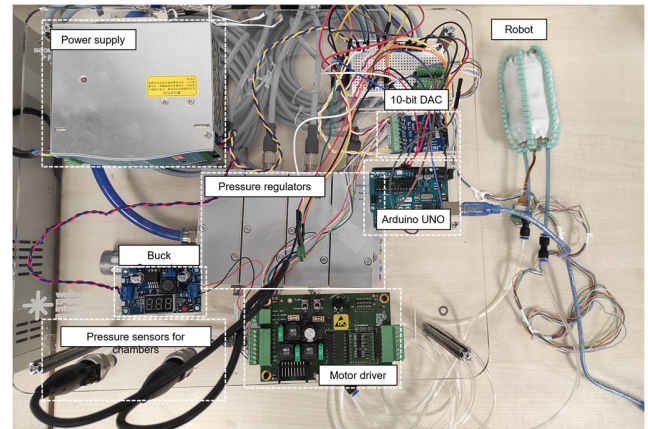


Figure 7 – Control setup for the robot with open loop scheme: the user sets the pressure of the two chambers with 2 pressure regulators through the analog input of the D/A converter and controls the brushless motor through the motor driver board. Pressure signals and speed of the motor are captured and processed with Arduino UNO board.

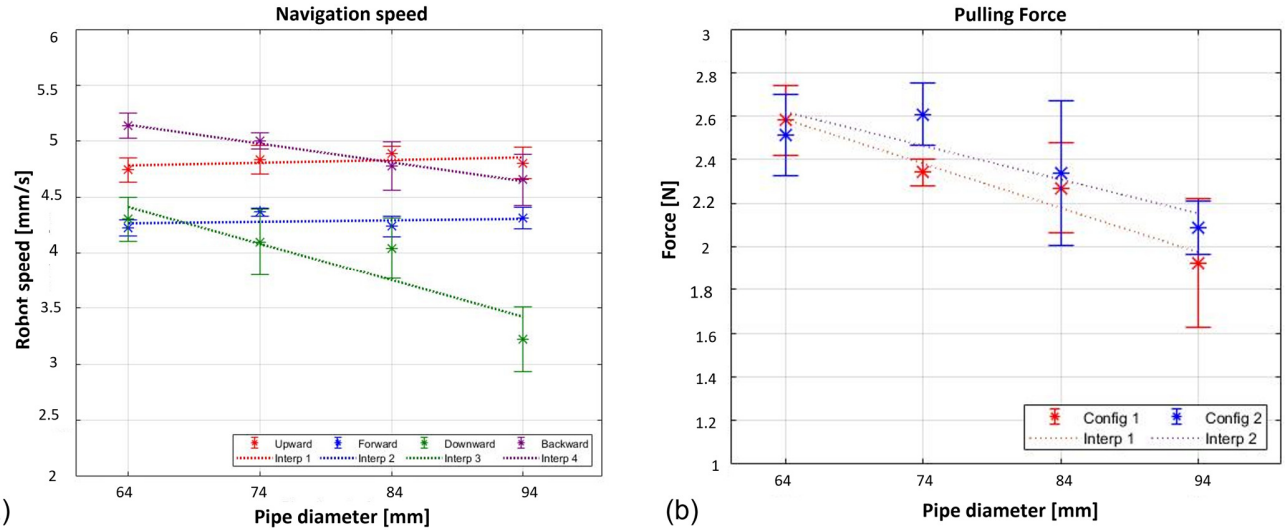


Figure 9- a) Speed of the robot at different diameters with interpolation curve and standard deviation, considering vertical climbing (upward and backward) and horizontal climbing (forward and backward). The vertical speed is mostly affected when the robot climbs 94 mm pipe. When crawling horizontal pipes at different outer diameters, the robot keeps its navigation velocity almost constant. (b) Pulling force results at different diameter, with interpolation curve and standard deviation. Two configurations of initial position are considered. In the first configuration (Config 1), the angle between the track and the vertical axis is almost 0° . In the other configuration (Config 2), the vertical axis lies between two consecutive track and the relative angle between the vertical axis and the tracks is around 30° .

overall diameter by more than 50% when navigating in the 94 mm pipe. The pressure of the two chambers is tuned initially to stabilize the robot with all the tracks in contact and all the experiments are conducted under the same level of inflation according to the diameter of the navigated pipe; pressure values of the chambers for the different diameters are presented in Table 2.

On one hand, the maximum vertical speed of the robot decreases with the increment of the diameter of the pipe, resulting in a more significant reduction when the system navigates inside the 94 mm diameter pipe. This is partially due to the additional friction introduced by the higher contact force between tracks and chambers. On the other hand, the

horizontal velocity of the robot, that peaks at 4.89 ± 0.06 mm/s, does not vary significantly across the different geometries tested. This is because the system can be kept at a slightly lower pressure than in the vertical scenario because it does not need to ensure stable grasping of all the tracks to prevent the robot from falling, hence, the friction losses are lower.

The tests conducted validated the proposed design solution, showing that the system can easily navigate pipes of different diameter even in the extreme case of fully vertical navigation.

B. Pulling force experiment

The stall pulling force exerted by the robot is measured as well for different pipe diameters to evaluate the payload capabilities of the system. To do so, the front of the robot is connected to a load cell through an inextensible tendon in series with a spring, the robot is pressurised to match the lumen of the pipe navigated and then it moves backward to pull the wire.

The testing rig is presented in Fig. 10. The force is measured by the load cell until displacement of the robot is no longer observed and two initial configurations were considered for this test: first configuration considers the robot standing on the track in correspondence of the vertical axis, while in second configuration, the vertical axis lies between two consecutive tracks.

Five measurements for each diameter and for each configuration are collected, with the motor running at 5000 RPM, to avoid large inertial forces in the tests. Results for the two cases are presented in Fig. 9b: the stall force slightly decreases in a larger diameter, from a maximum of 2.60 ± 0.14 N for 74 mm diameter pipe to almost 1.92 ± 0.30 N force for 94 mm diameter and no significant variation of the stall force between the two configurations is detected, highlighting that the symmetry of the tracks provides homogeneous traction force distribution.

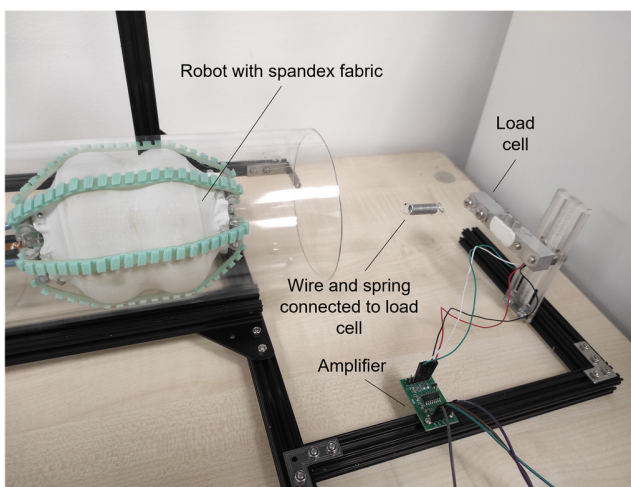


Figure 10- Stall force experiment of the robot (with Spandex fabric embedded) inside an acrylic pipe in a 94 mm ID (internal diameter) horizontal pipe. The force is measured by the load cell connected to the robot through a wire and spring: the robot is pressurized to match the lumen of the pipe, then it moves backward to pull the wire.

IV. CONCLUSION AND FUTURE WORK

In this work we propose a novel design for robotic system for in-pipe navigation and inspection that exploits the use of multiple soft elastic materials to enable shape-shifting capabilities to adapt to a wide range of pipe geometries. We validated the locomotion capability of the proposed proof-of-concept system in acrylic pipes and demonstrated that a single DOF track-based locomotion can be achieved, regardless of the level of inflation of the chambers, hence, of the overall geometry of the system.

It is also worth noticing that the traction force of the system is directly related to the wall-pressing force produced by the inflation of the chambers, thus another desirable measurable feedback to embed to reliably control this system could be obtained by either the pressure feedback from the two pressure lines or from dedicated flexible sensors to embed in the walls of the chambers. On this note, acrylic pipes were selected as worst-case scenario for testing given their perfectly smooth surface; the locomotion inside rough irregular surface may result significantly more efficient.

Future work will investigate the use of the proposed system in different scenarios, including pipe with partial obstructions and pipe with running fluids. Another important area that we are planning to investigate is the use of the proposed system in clinical application, in specific for inspection of the gastro-intestinal tract. The shape-shifting capability of this system paired with its elastic interface can provide an optimal navigation solution for soft flexible pipe-like structures like the colon that typically varies in diameter from the rectum to the cecum by more than 150%. Both for clinical and industrial applications future work will focus on miniaturising the proposed system to access smaller lumens.

V. ACKNOWLEDGEMENT

This research was funded in whole, or in part, by the Wellcome/EPSRC Centre for Interventional and Surgical Sciences (WEISS) [203145/Z/16/Z]; the Engineering and Physical Sciences Research Council (EPSRC) [EP/P027938/1, EP/R004080/1, EP/P012841/1]; the Royal Academy of Engineering Chair in Emerging Technologies Scheme [CiET1819/2/36] and by the Rosetrees Trust/Stoneygate Trust Enterprise Fellowship Scheme [M884]. For the purpose of open access, the authors have applied a CC BY public copyright licence to any author accepted manuscript version arising from this submission.

REFERENCES

- [1] B. B. V. L. Deepak, M. V. A. R. Bahubalendruni, and B. B. Biswal, “Development of in-pipe robots for inspection and cleaning tasks: Survey, classification and comparison,” *International Journal of Intelligent Unmanned Systems*, vol. 4, no. 3. 2016, doi: 10.1108/IJIUS-07-2016-0004.
- [2] L. Shao, Y. Wang, B. Guo, and X. Chen, “A review over state of the art of in-pipe robot,” *2015 IEEE Int. Conf. Mechatronics Autom. ICMA 2015*, pp. 2180–2185, 2015, doi: 10.1109/ICMA.2015.7237824.
- [3] M. Han, J. Zhou, X. Chen, and L. Li, “Analysis of In-Pipe Inspection Robot Structure Design,” 2016, doi: 10.2991/wartia-16.2016.210.
- [4] A. Gmíterko, I. Virgala, L. Miková, P. Frankovský, T. Kelemenová, and M. Kelemen, “Machines for In-Pipe Inspection,” *J. Autom. Control*, vol. 3, no. 3, pp. 79–82, 2015, doi: 10.12691/automation-3-3-8.
- [5] C. Jun, Z. Q. Deng, and S. Y. Jiang, “Study of locomotion control characteristics for six wheels driven in-pipe robot,” *Proc. - 2004 IEEE Int. Conf. Robot. Biomimetics, IEEE ROBIO 2004*, pp. 119–124, 2004, doi: 10.1109/robio.2004.1521762.
- [6] A. Kakogawa, S. Ma, and S. Hirose, “An in-pipe robot with underactuated parallelogram crawler modules,” *Proc. - IEEE Int. Conf. Robot. Autom.*, pp. 1687–1692, 2014, doi: 10.1109/ICRA.2014.6907078.
- [7] D. Chablat, S. Venkateswaran, and F. Boyer, “Mechanical Design Optimization of a Piping Inspection Robot,” 2018, doi: 10.1016/j.procir.2018.02.015.
- [8] A. Zagler and F. Pfeiffer, “‘MORITZ’ a pipe crawler for tube junctions,” 2003, doi: 10.1109/robot.2003.1242044.
- [9] G. Granosik and J. Borenstein, “The OmniTread serpentine robot with pneumatic joint actuation,” in *Proceedings of the Fifth International Workshop on Robot Motion and Control, RoMoCo’05*, 2005, vol. 2005, doi: 10.1109/romoco.2005.201409.
- [10] D. Rus and M. T. Tolley, “Design, fabrication and control of soft robots,” *Nature*, vol. 521, no. 7553. 2015, doi: 10.1038/nature14543.
- [11] P. Polygerinos *et al.*, “Soft Robotics: Review of Fluid-Driven Intrinsically Soft Devices; Manufacturing, Sensing, Control, and Applications in Human-Robot Interaction,” *Advanced Engineering Materials*, vol. 19, no. 12. 2017, doi: 10.1002/adem.201700016.
- [12] G. Singh, S. Patiballa, X. Zhang, and G. Krishnan, “A pipe-climbing soft robot,” 2019, doi: 10.1109/ICRA.2019.8793815.
- [13] G. Feng, W. Li, Z. Li, and Z. He, “Development of a wheeled and wall-pressing type in-pipe robot for water pipelines cleaning and its traveling capability,” *Mechanika*, vol. 26, no. 2, 2020, doi: 10.5755/j01.mech.26.2.18783.
- [14] H. Li, R. Li, J. Zhang, and P. Zhang, “Development of a pipeline inspection robot for the standard oil pipeline of china national petroleum corporation,” *Appl. Sci.*, vol. 10, no. 8, 2020, doi: 10.3390/APP10082853.
- [15] A. Kakogawa, T. Nishimura, and S. Ma, “Designing arm length of a screw drive in-pipe robot for climbing vertically positioned bent pipes,” *Robotica*, 2016, doi: 10.1017/S026357471400143X.
- [16] T. Li, S. Ma, B. Li, M. Wang, Z. Li, and Y. Wang, “Development of an in-pipe Robot with differential screw angles for curved pipes and vertical straight pipes,” *J. Mech. Robot.*, 2017, doi: 10.1115/1.4037617.
- [17] L. Qingyou, R. Tao, and Y. Chen, “Characteristic analysis of a novel in-pipe driving robot,” *Mechatronics*, vol. 23, no. 4, pp. 419–428, 2013, doi: 10.1016/j.mechatronics.2013.03.004.
- [18] S. Iwashina, I. Hayashi, N. Iwatsuki, and K. Nakamura, “Development of in-pipe operation micro robots,” *Proc. Int. Symp. Micro Mach. Hum. Sci.*, pp. 41–45, 1994, doi: 10.1109/ismmhs.1994.512896.
- [19] J. H. Kim, G. Sharma, and S. S. Iyengar, “FAMPER: A fully autonomous mobile robot for pipeline exploration,” 2010, doi: 10.1109/ICIT.2010.5472748.
- [20] Y. S. Kwon and B. J. Yi, “Design and motion planning of a two-module collaborative indoor pipeline inspection robot,” *IEEE Trans. Robot.*, 2012, doi: 10.1109/TRO.2012.2183049.
- [21] A. Singh, E. Sachdeva, A. Sarkar, and K. M. Krishna, “COCrIP: Compliant OmniCrawler in-pipeline robot,” 2017, doi: 10.1109/IROS.2017.8206446.
- [22] J. Dai, Y. Xu, and W. Zhang, “SPC ROBOT: A novel pipe-climbing robot with spiral extending of coupled differential,” 2018, doi: 10.1109/ROBIO.2017.8324562.
- [23] K. Sato, T. Ohki, and H. O. Lim, “Development of in-pipe robot capable of coping with various diameters,” *Int. Conf. Control. Autom. Syst.*, pp. 1076–1081, 2011.
- [24] D. Fang, J. Shang, Z. Luo, P. Lv, and G. Wu, “Development of a novel self-locking mechanism for continuous propulsion inchworm in-pipe robot,” *Adv. Mech. Eng.*, vol. 10, no. 1, pp. 1–11, 2018, doi: 10.1177/1687814017749402.
- [25] I. Virgala, A. Gmíterko, and M. Kelemen, “Motion Analysis of In-pipe Robot Based on SMA Spring Actuator,” *J. Autom. Control*, vol.

1, no. 1, pp. 21–25, 2013, doi: 10.12691/automation-1-1-4.

[26]O. Ostertag, E. Ostertagová, M. Kelemen, T. Kelemenová, J. Buša, and I. Virgala, “Miniature mobile bristled in-pipe machine,” *Int. J. Adv. Robot. Syst.*, vol. 11, pp. 1–9, 2014, doi: 10.5772/59499.

[27]H. Heung, P. W. Y. Chiu, and Z. Li, “Design and prototyping of a soft earthworm-like robot targeted for GI tract inspection,” *2016 IEEE Int. Conf. Robot. Biomimetics, ROBIO 2016*, pp. 497–502, 2016, doi: 10.1109/ROBIO.2016.7866371.

[28]X. Zhang, T. Pan, H. L. Heung, P. W. Y. Chiu, and Z. Li, “A Biomimetic Soft Robot for Inspecting Pipeline with Significant Diameter Variation,” *IEEE Int. Conf. Intell. Robot. Syst.*, pp. 7486–7491, 2018, doi: 10.1109/IROS.2018.8594390.

[29]T. Yamamoto, S. Sakama, and A. Kamimura, “Pneumatic Duplex-Chambered Inchworm Mechanism for Narrow Pipes Driven by only Two Air Supply Lines,” *IEEE Robot. Autom. Lett.*, vol. 5, no. 4, 2020, doi: 10.1109/LRA.2020.3003859.

[30]M. D. Gilbertson, G. McDonald, G. Korinek, J. D. Van De Ven, and T. M. Kowalewski, “Serially Actuated Locomotion for Soft Robots in Tube-Like Environments,” *IEEE Robot. Autom. Lett.*, 2017, doi: 10.1109/LRA.2017.2662060.

[31]L. Manfredi, E. Capoccia, G. Ciuti, and A. Cuschieri, “A Soft Pneumatic Inchworm Double balloon (SPID) for colonoscopy,” *Sci. Rep.*, vol. 9, no. 1, pp. 1–9, 2019, doi: 10.1038/s41598-019-47320-3.

[32]K. Suzumori, T. Miyagawa, M. Kimura, and Y. Hasegawa, “Micro inspection robot for 1-in pipes,” *IEEE/ASME Trans. Mechatronics*, vol. 4, no. 3, pp. 286–292, 1999, doi: 10.1109/3516.789686.

[33]D. Kim, D. Lee, B. Kim, and B.-I. Lee, “A self-propelled robotic colonoscope using elastic caterpillars,” in *IEEE ISR 2013*, 2013, pp. 1–4.

[34]G. A. Formosa, J. M. Prendergast, S. A. Edmundowicz, and M. E. Rentschler, “Novel Optimization-Based Design and Surgical Evaluation of a Treaded Robotic Capsule Colonoscope,” *IEEE Trans. Robot.*, 2019.

[35]A. Menciassi, S. Gorini, G. Pernorio, W. Liu, F. Valvo, and P. Dario, “Design, fabrication and performances of a biomimetic robotic earthworm,” 2004, doi: 10.1109/robio.2004.1521789.

[36]S. Kim, M. Spenko, S. Trujillo, B. Heyneman, V. Mattoli, and M. R. Cutkosky, “Whole body adhesion: Hierarchical, directional and distributed control of adhesive forces for a climbing robot,” 2007, doi: 10.1109/ROBOT.2007.363159.

[37]B. Mosadegh *et al.*, “Pneumatic networks for soft robotics that actuate rapidly,” *Adv. Funct. Mater.*, vol. 24, no. 15, 2014, doi: 10.1002/adfm.201303288.

[38]V. Consumi, L. Lindenroth, D. Stoyanov, and A. Stilli, “SoftSCREEN-Soft Shape-shifting Capsule Robot for Endoscopy based on Eversion Navigation,” doi: 10.12809/hkmj154685.

[39]L. Marechal, P. Balland, L. Lindenroth, F. Petrou, C. Kontovounisios, and F. Bello, “Toward a Common Framework and Database of Materials for Soft Robotics,” *Soft Robot.*, vol. 00, no. 00, 2020, doi: 10.1089/soro.2019.0115.

APPENDIX

In terms of power transmission, the direct interaction between the teeth of the worm gear and the teeth of the tracks is extremely useful when the motor operates at a high rotational speed with low torque while the desired transmission output has low speed with high torque, as in this case.

In the proposed system the driving member consists of a rigid, cylindrical, and straight worm gear with a helicoidal single-head thread profile, whilst the driven member is a closed-loop elastic track. For the calculation presented in this section please refer to Fig. 2a.

The proposed system has only 1 DOF: by changing the direction of rotation of the motor shaft, the direction of the linear motion of the robot can be set as forward or backward.

Any of the teeth of the portion of the tracks engaged with the worm gear will move with a linear speed v_t in the direction of the main axis of symmetry of the system according to

$$v_t = \frac{\omega p}{2\pi} \quad (4)$$

Here p is the pitch of the worm gear and ω is the angular velocity of the worm gear expressed in rad/s . We are considering an ideal, yet realistic scenario where once the teeth are engaged, they cannot slip out of the thread of the worm gear and that no tooth will be skipped.

Given the normal reaction force N applied by the thread at the interface with the track, the lead angle θ of the thread, and the friction coefficient μ between the worm gear and track, the axial force F_a applied by the worm gear on each track is given by equation (2).

$$F_a = N \cos \theta - \mu N \sin \theta \quad (5)$$

Considering D_w the pitch circle diameter of the worm gear and T the reacting torque acting on the worm gear, the tangential force F_t provided by the motor is:

$$F_t = \frac{2T}{D_w} = N \sin \theta + \mu N \cos \theta \quad (6)$$

Similarly to the model presented in [33], if we consider T_0 the saturation torque of the motor, T_f the friction torque and ω_0 its no load velocity, $F_{a_{MAX}}$, the maximum thrust force of the robot and the velocity of the robot v_r can be expressed with respect to the torque as follows:

$$F_{a_{MAX}} = \frac{2(\pi D_w - \mu p)(T_0 - T_f)}{D_w(\mu\pi D_w + p)} \quad (7)$$

$$v_r = \frac{p\omega_0}{2\pi} \left[1 - \frac{1}{T_0} \left(\frac{(\mu\pi D_w + p)F_a D_w}{2(\pi D_w - \mu p)} \right) + T_f \right] \quad (8)$$

In our system, due to the elasticity of the members involved in the power transmission, i.e. the tracks, part of the mechanical energy provided by the motor will be used to deform the elastic material of the tracks and dissipated. Further energy dissipation will occur due to friction between sliding elements, including the sliding of the lateral surface of the teeth on the lateral surface of the thread of the worm gear, the sliding between the surface of the chambers and the flat base of the tracks as well as of the smaller portion of energy dissipated by the movement of the tracks on the series of bearings embedded in the internal part of the chassis to guide the portion of the tracks engaged with the worm gear. It is also important to note that the worm gear profile and the tracks profile of the proposed system is designed so that only one of the two sides of each tooth of the tracks is in contact with the thread, while the other side and the head of each tooth are not, in order to increase the efficiency of the transmission minimizing energy dissipation associated with sliding.